Development of a rigorous simulation model of geothermal power plants for emission control

Marco Vaccari[a], Gabriele Pannocchia[a,c], Leonardo Tognotti[a], Marco Paci[b], Roberto Bonciani[b]

[a]*Department of Civil and Industrial Engineering, University of Pisa, Pisa, Italy*
[b]*Enel Green Power*
[c]*Corresponding author: gabriele.pannocchia@unipi.it*

Abstract

Geothermal power plant (GTPP) operating conditions and associated emissions mainly depend on the endogenic fluid used to generate power, and the case of GTPPs located in Tuscany (Italy) is considered in this study. Since measuring on-line the quantity of emitted pollutants is a difficult task, a process simulation model featuring all unit operations of the GTTP is developed using UniSim Design® to forecast and control pollutant emissions. An accurate identification of the thermodynamic correlation parameters for the solubility of the considered pollutants (mercury and hydrogen sulfide) in water has been performed to match literature values. A data reconciliation procedure is used to match the simulation model outcome with real measurements of two (20MWe and 40MWe) GTTPs. Results are fully satisfactory as the mercury emission forecasted is always slightly above the measured data, evidencing the model is conservative, and hence reliable in ensuring satisfaction of emission limits established by law. For the 20MWe plant, the simulated total mercury emissions are 3.31 g/h exceeding the measured ones by 27%, while for the 40MWe plant, they are 1.38 g/h above the measured ones by 4%. In addition, for the 20MWe plant, pollutants emission and net power production are both considered in a performance analysis. The worst case scenario for power generation (18.7MW) is in summer conditions, while for pollutant emission is in winter conditions with 5.22 g/h of total mercury and 20.46 kg/h of hydrogen sulfide. Finally, energetic performances result to be independent from the environmental measures adopted.

Keywords: Geothermal System, Geothermal Power Plant, Modeling, Simulation, Environment.

1. Introduction

Geothermal power generation represents a green and widely spread technology to produce electricity [1], and regionally coordinated approaches could even increase the geothermal exploitation to cover a significantly larger part of the current heat demand, focusing on optimizing the recovery efficiency. The authors in [2] use the West Netherlands Basin region as case study to underline how tailor-made financial and legislative mechanisms are required to promote more efficient use of geothermal resources. Solutions that use a geothermal system to augment the performance of a fossil fuel based power plant can be found in [3], in which the best configuration is sough in order to exploit low-enthalpy geothermal heat to preheat feed-water in coal-fired power plants by replacing some of the high-grade steam that can then be used to generate more power.

The impact of geothermal power is often considered as environmentally friendly, and different national standards evaluate the environmental effect of power plants depending on the resource utilized. A recent discussion about potential role of geothermal power generation technologies in a sustainable future is reported in [4]. Environmental effects linked to geothermal power plants are mostly associated with emissions at the site, rather than, for instance, hidden in the manufacturing process of plant components or governed by drilling activities. Atmospheric emissions, especially of fugitive greenhouse gases (GHG), should be deeply investigated and compared with any natural emissions from the soil present in the geothermal area [5]. Environmentally sustainable management of geothermal power generation still represents a challenge. Hence, life cycle environmental studies can be helpful to develop this industrial sector [6].

Since 1970s', geothermal energy in the Mt. Amiata (Italy) area is used to generate electric power. Uncommonly high levels of mercury characterize geothermal fluids of Mt. Amiata, an area renowned for its vast cinnabar deposits

and for the mercury production carried out in the past [7]. Hence, due to the characteristics of the endogenic fluid, a particular problem for geothermal power plants (GTPPs) is represented by the presence of mercury in addition to other common pollutants like hydrogen sulfide, as studied by Loppi [8]. A recent comprehensive environmental impact assessment for the calculation of atmospheric emissions connected with the operational phase of the GTTPs in Tuscany has evidenced that mercury still represents a critical problem for all the geothermal fields [9]. Multiple environmental monitoring and mitigation measures have been put in action in Italy to maintain impact values below the thresholds defined by European and Italian laws [10]. Real-time measurements of mercury allow to recognize its air concentration variability, providing a more realistic picture than that obtained by using passive traps [11], and different standardized methods for the analytical determination of mercury are currently used by the authority [12, 13, 14]. However, analyzing the data reported by the Tuscany Regional Agency for Environmental Protection (ARPAT), a significant level of variability in the analytical determination of the emissions is evidenced [9], most likely due to the very low concentration of mercury and the technical difficulties related to various sampling procedures. For all such reasons, the geothermal operator Enel Green Power (EGP) has undertaken a series of actions aimed at characterizing in a more accurate and reproducible way the emissions of mercury exiting the plant, and, at same time, at supporting the analytical evaluations with methodologies and modeling tools.

Hence, this paper presents a detailed process simulation model, developed on the basis of the real data of GTPPs provided by EGP, aimed mainly at evaluating mercury emissions from evaporative towers as the operating and environment conditions of GTPPs vary.

2. The geothermal process

2.1. The geothermal cycle

The process layout to be used for power generation depends on the conditions of the well-water geothermal fluid. If the fluid is in the vapor state, it can be used directly: steam is sent firstly into a turbine, coupled to an electric generator, and then to a condenser downstream of which the condensate is re-injected into the well. More often, the fluid appears as a mixture of liquid and vapor, hence a separation of the liquid fraction before sending the steam into the turbine is required. Since very often it is convenient to associate a flash unit to the separation of the vapor phase from the liquid phase, this system is called "flash plant". As the fraction of liquid increases, or in the presence of geothermal fluid consisting solely of liquid water, a flash plant technology is no longer convenient, and better performance is achieved by adopting a so-called "binary" cycle, in which the conversion of thermal in mechanical power takes place in a completely separate circuit.

Many works in the literature analyze both configurations to maximize the produced electric power in terms of energy and exergy. A performance evaluation study for a single flash cycle was performed for a GTPP located in Turkey [15], whereas Jalilinasrabady et al. [16] suggested to introduce a double flash cycle for a GTPP located in northwest Iran in order to minimize exergy losses. As well as for single flash cycles, also binary cycles GTPPs have been deeply studied in literature [17, 18]. The exergy analysis for the GTPPs is used to identify and quantify the sites of exergy destruction so as to pinpoint where performance improvement should be assessed. Data values from a double-flash system GTTP have been used to identify the exergy losses along the whole plant [19], whereas different possible thermal optimization solutions of double-flash GTTPs, by the means of additional heat exchangers properly located in the system, have been analyzed [20]. The performance of the double-flash system based on energy and exergy analyses, have also been used to study the possible upgrade of an existing single-flash GTTP in Indonesia [21]. Simulation analysis has also been used to evaluate new possible Organic Rankine Cycle (ORC)-binary power plants using less data and with a high accuracy [22]. Exergo-economic performance indicator of a (ORC)-binary GTTP have also been used to compare economic performance with thermodynamic efficiency of the plant [23, 24]. A recent work proposed an optimization approach for a (ORC)-binary GTTP using various combinations of azeotropic mixtures as working fluid [25], by means of a Particle Swarm Optimization (PSO) algorithm. Possible improvements of a GTTP with flash-binary system using a double flash system, together with a thermo-economic evaluation, have been explored in [26]. Performance evaluation of GTTP in terms of pollutants emitted has also been explored in [27], where the authors analyze which is the best solution for an existing plant among a double flash, single flash-binary and double flash-binary layouts, in order to obtain the maximum output power and the lowest excess deposit of silica. Furthermore, tools for selecting optimum power generation cycles used for GTTPs based on a detailed analysis of the

Nomenclature

Acronims

AMIS® Mercury and Hydrogen Sulphide abatement system

BG3 GTTP Bagnore 3

EGP ENEL Green Power

EOS Equation of State

GHG Greenhouse Gases

GTPP Geothermal Power Plant

ORC Organic Rankine Cycle

PFD Process Flow Diagram

PR Peng-Robinson

RAD GTPP Nuova Radicondoli

Symbols

$\mathscr{H}_{Hg}$ Henry's constant for mercury

b, a_i, a_j Terms referring to the critical thermodynamic quantities of the individual substances of the mixture

$Comp$ Composition

F Flow

F_{23} Volumetric flow of stream *23*

k_{ij} Interaction coefficient between two species i and j

L/G Vapor liquid Ratio

N Number of components of a mixture

N_S Number of $TOWER$ stages

P Pressure

p^0 Saturation pressure

R Standard gas constant

T Temperature

T_{13} stream *13* temperature

T_{15} stream *15* temperature

U_{13} stream *13* humidity

V Volume

w_i Mass fraction of i-th specie

x_{Hg} Molar fraction of mercury in liquid phase

y_{Hg} Molar fraction of mercury in gaseous phase

Greek Letters

Δ Percentage deviation of the considered variable from its target

η_S *TOWER* stages efficiency

η_K *K-100* and *K-101* efficiencies, gas extractor compression stages

ξ_{TEE} split *TEE-100* multiplier parameters

Φ Data reconciliation objective function

ϕ_i value of i-th variable at a given instant

$\bar{\phi}_i$ reference value for i-th variable

Subscripts

max maximum

min minimum

aq aqueous

g gaseous

l liquid

Hg related to Mercury

thermodynamic performance are available in literature [28]. An extensive survey on performance evaluation of both single flash and binary cycles can be found in [29]. Finally, the reader isreferred to a recent and detailed review on the state-of-the-art of power production using geothermal energy, system design and optimization [30].

2.2. The considered GTPP and the equipment used

The geothermal power plants of the type currently used in Italy are those with a direct steam condensation cycle and release into the atmosphere the noncondensable gases associated with the geothermal fluid that feeds them. Figure 1 depicts a simplified process flow diagram (PFD) of the GTPP taken as reference in this work. The endogenous fluid produced by various wells is conveyed to the GTPP by means of a network of vapor ducts and expanded in a turbine, at the outlet of which the steam enters a direct mixing condenser maintained in vacuum conditions. The noncondensable gases contained in the geothermal fluid, are extracted from the condenser by means of a multi-stage

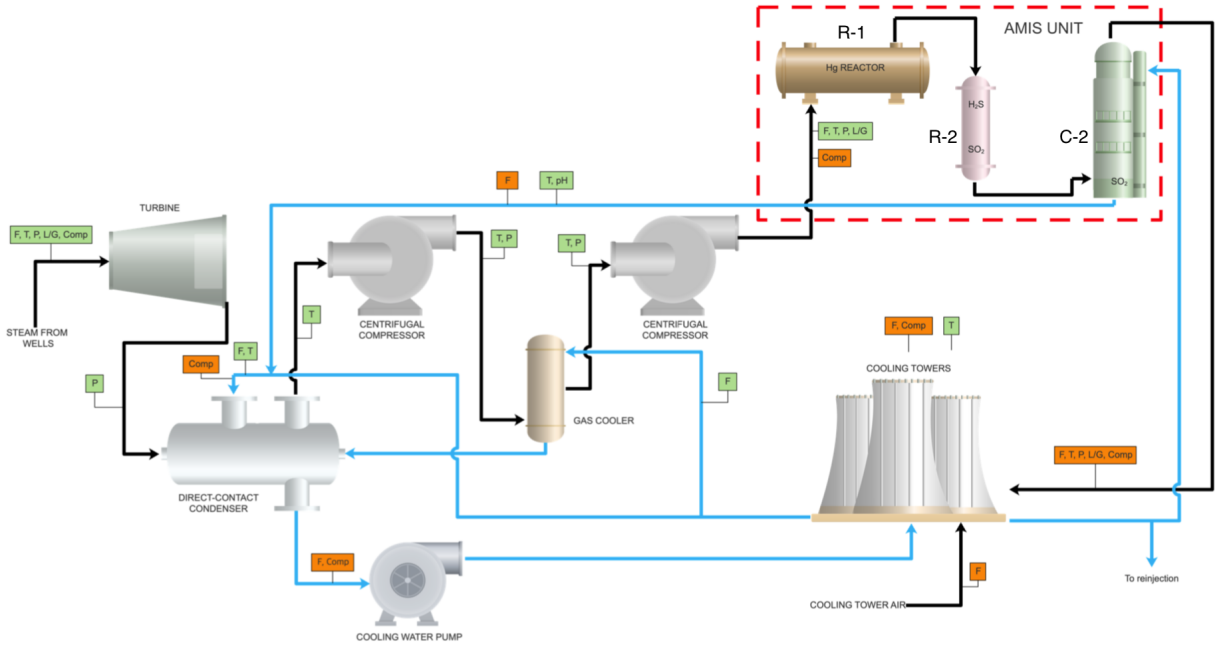

Figure 1: Scheme of the measurements made in the central unit. Legend: Blue lines represent water, green measurements are made in continuous, orange ones are made on spot.

centrifugal compressor and conveyed to the mercury and hydrogen sulphide abatement system (AMIS®) [31]. This gaseous stream is composed by the substances originally present in the geothermal fluid in the vapor phase (CO_2, CH_4, H_2S, N_2, O_2, H_2, Ar) and other substances which, at the process conditions, remain in the vapor phase, such as water and Hg. The AMIS® system consists mainly of two parts: one cold (Hg blast chiller) and one hot (H_2S blast chiller). The incoming gas is cooled down in a tower from 200 °C to about 30 °C to enter an activated carbon Hg absorber impregnated with sulfur and/or selenium mass (R-1); the residual gas stream is the reheated in a heat exchanger to bring the stream temperature up to $200 - 250$ °C necessary for the reactor R-2 where the oxidation of H_2S to SO_2 occurs; finally, the SO_2 is removed by washing out the gas stream in a packed column (C-2).

The gaseous stream exiting the abatement system is conveyed, by means of a pipe, to the base of the cooling tower assembly. This consists of three wet type cells for each 20 MW group, with induced or natural draft for the dispersion into the atmosphere. The water obtained from steam condensation, mixed with the cooling one, exits the condenser and it is sent, via an extraction pump, to a distribution system on the chimneys of the cooling tower. In the towers, the water coming from the steam condensation is cooled down (in countercurrent) by an ascending flow of natural air or induced by fans which work at constant number of revolutions. Part of this water evaporates (about $19 - 25$ kg/s) while the remainder, cooled down to about 30 °C, is sent to the collection tank, from which it takes different routes. Part of it is used as cooling fluid in the mixing condenser and in the intercooler stage of the gas extractor, another part is sent to the AMIS® system as washing fluid of the C-2 column, and the remainder is re-injected into the wells through specific aqueducts.

2.3. The operating conditions and their variability

Cooling tower fans and gas extractor motors work at constant revolutions, and this induces a certain seasonality of the operating conditions to the condenser. Since vacuum of this apparatus is maintained only by the gas draft of the extractor, when the ambient temperature changes, the pressure will respond accordingly, passing from 40 mbar in winter to 120 mbar during summer. This obviously has repercussions on the operating conditions of the plant and on the quantities emitted. Between the liquid and the gaseous stream exiting the condenser, there is an average temperature difference of about $2 - 3$ °C depending on the sensitivity of the appliance. The measured temperatures

are therefore around $30-37$ °C for the hot water and $27-34$ °C for the gases entering the extractor. The evaporative towers work in conditions that strongly depend on the seasonality: both the temperature and the humidity of the atmospheric air intake greatly affect the amount of water evaporated and, consequently, the temperature of the cooled water. Hence, the excess water from the towers has usually a temperature around 25 °C with peaks that can reach $30-35$ °C in the warmer seasons. This greatly affects the process performances because it influences the equilibria that are established at the condenser and, consequently, the amount of Hg and H_2S that takes the path toward the AMIS® abatement system. The scheme of the measurements that are normally available in the central is also shown in Figure 1. As can be seen from Figure 1, most of the composition measurements are made in spots, i.e. during the usually half-yearly measurement campaigns. The compositions are obviously measured at the process input, at the input and output of the AMIS® system, and at the input and output of the cooling towers. The endogenous fluid entering the plant can have a certain variability linked to the fact that its origin can be diversified. In other words, in the course of its life, it is possible that the plant is powered by different wells, both for reasons of maintenance of the vapor ducts and for regeneration of the wells themselves.

3. Atmospheric emissions and the fate of pollutants

Due to the different geological characteristics of the geothermal fields in Tuscany, fluids have significantly different compositions, temperature and pressure, and consequently a different emission profile in the atmosphere, as well as different treatment capacities and abatement of pollutants of the associated GTTPs. The typical fluid from Larderello area consists of superheated steam with a high content of hydrogen sulphide (H_2S) and chlorine (Cl). On the other hand, the fluid of the Mt. Amiata area is a saturated vapor at high pressure and with a high content of noncondensable gases; the concentration of H_2S is lower than that of the Larderello area but the fluid is also rich in other pollutants. The emissions of the Larderello area are greater due to the greater installed power, but almost all pollutants affect the Mt. Amiata area. It is worth mentioning the presence of the minero-metallurgical activity of cinnabar on Mt. Amiata, that contributed to a surplus of Hg already present in the territory, so that today it is not possible to distinguish between anthropic mercury and naturally occurring one. Another peculiarity of the Amiata geothermal fluid is the nonnegligible presence of ammonia. The emissions in air, in GTPPs of this type, are therefore mainly linked to the line of noncondensable gases and to the aerator of the condensation tower, gaseous streams that gather in the cooling tower to be emitted into the atmosphere. The line of noncondensable gases collects gaseous substances naturally present in the geothermal fluid, such as H_2S, CO_2, CH_4, N_2, Ar, O_2, H_2 and Hg vapors. The gaseous phase of the condensation tower, on the other hand, is an aerosol of substances such as NH_3 and As partially evaporated and stripped from the drops in the cooling towers. The aerosol substances thus formed undergo drift outside the refrigeration tower and fall close to the plant, unlike the gaseous emissions that can spread in much larger areas. In the last 15 years approximately, AMIS® systems have been introduced in all GTPPs, which act on the line of noncondensable gases to reduce H_2S and Hg emissions. On the other hand, for years, aerosol elimination systems dragged into the towers (demister) are active, so that the problem of entrained aerosol spills has been solved.

From the authority point of view, there is no specific European or national legislation that sets limit values or alarm thresholds for all substances emitted in the context of GTPPs. A first legislative attempt to regulate emission from plants using geothermal fluids, sets limit values depending on a threshold for mass flow: the pollutant mass flow must first be measured or calculated and its value compared with standards. Consequently, only if the measured mass flow is equal to or greater than the imposed threshold, the concentration limit is applicable. Waiting for a comprehensive and updated regulatory framework, the Tuscany Region has regulated on this matter defining specific requirements for new GTPPs and for renewing the relevant authorizations by setting emission limits, both as an absolute value and as a pollutants abatement efficiency, consistent with the emission framework of the plants and taking into account the current state of the technologies. On the other hand, the emissions of a GTPP depend on the amount of fluid entering the plant, hence the power of the plant itself. Hence, with reference to these parameters, the Tuscany Region introduced specific, more stringent and verifiable limits with respect to those established by the state legislation. At the same time, the monitoring of the plants should be carried out continuously, but this is not possible due to operational difficulties. In this scheme, it is clear how a method to estimate the emitted pollutants is strongly needed both for the GTPP owners but also for legislations representatives.

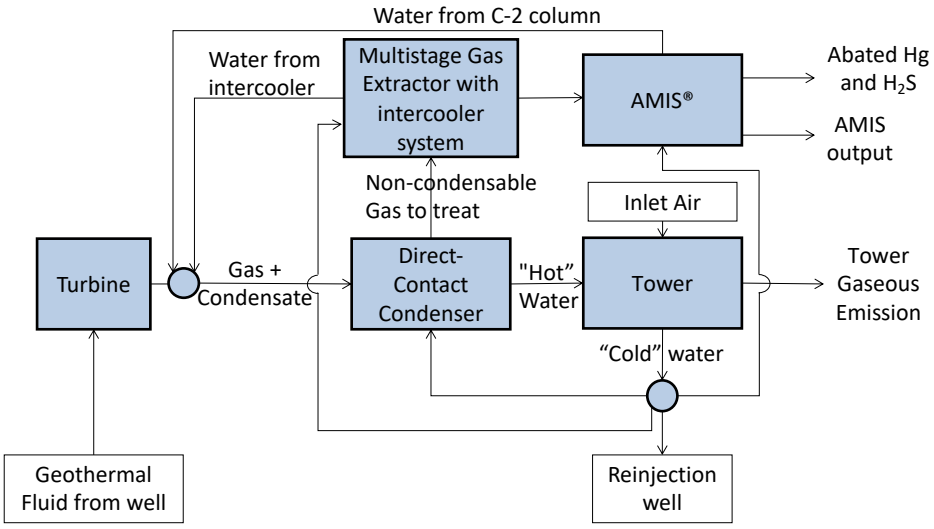

Figure 2: Block diagram of the simulated geothermal process. The dots represent mixer or splitters of the streams.

4. Power plant model

In order to evaluate the emissions of mercury from the evaporative towers of a GTPP, a detailed process simulation model is built, in order to be able to analyze the route and the distribution of the pollutant among the various unit operations as operating and process conditions change. In this way it is also possible to study the propagation of the uncertainties on the most significant parameters in the permitted ranges of variation of the operating and process conditions. The actual implementation of a GTPP represents specifically the 20 MWe Bagnore 3 plant, in the Mt. Amiata area. Subsequently, the model has also been adapted to the 40 MWe Nuova Radicondoli plant, in the Larderello area.

There are many process simulation software, often of different nature. Two major branches are those represented by Aspen Plus® / Dynamics and Aspen HYSYS / UniSim Design®. From a user perspective, HYSYS / UniSim Design are often preferable to Aspen Plus because they offer a higher degree of flexibility combined with a coherent and logical approach to how the various functionalities are made available to the user, especially for highly interconnected processes, as the GTTPs. Being our purposes to follow the path of pollutants along the GTPP process, the choice of a HYSYS / UniSim simulation software is justified and, specifically, UniSim Design® is the software chosen in this work.

4.1. Conceptual model

The GTTP process consists of five basic sections as depicted with the block diagram shown in Figure 2. For each of them specific assumptions have been made. The section where the geothermal fluid entering the plant is expanded has been represented by a constant efficiency turbine. The direct-contact condenser is considered as a single equilibrium stage and therefore schematized with a flash tank where the two-phase streams enter to be separated into liquid and gas streams. The liquid outlet from the condenser (the "hot" water) is sent through a handling pump to the evaporative cooling towers. The pump has been simulated at constant efficiency. The gas stream coming out from the condenser needs to be treated to remove Hg and H_2S; hence, it is firstly compressed to atmospheric pressure and then sent to the AMIS® system. This compression is accomplished by two stages with intermediate cooling taking place in a flash tank where a portion of the "cold" water recycle from the evaporative towers arrives. Each compression stage is represented by a constant efficiency compressor. The AMIS® system has been considered as a "black box" that knocks down both Hg and H_2S flow-rates with two different, constant efficiencies. The emissions of Hg from the evaporative towers and from the AMIS® plant are, therefore, considered separately. Hence, three streams exit from AMIS: one containing precisely the abated Hg and the H_2S, the residual gas considered as emission, and the residual

Table 1: Input values necessary for the construction of the model.

Section	Item
multirow3*Turbine	Endogenous fluid: F, T, P, composition Turbine efficiency Turbine exhaust pressure
Handling pump	Pump efficiency Delivery pressure of the pump
Gas extractor	Compressor efficiency (I and II stage) Compressor discharge pressure (I and II stage)
AMIS plant	Reduction efficiency: Hg and H_2S Two-phase wash stream: T, P
Evaporative tower	Tower: number of stages, stadium efficiency, head and tail pressures Inlet air: F, T, P, relative humidity Partition coefficients of the liquid stream leaving the tower.

liquid recycled to the direct-contact condenser. Finally, the three-cell evaporative cooling tower system is considered as a multi-stage equilibrium absorption tower with constant efficiency.

It is necessary to underline how normally the residual gaseous stream coming out of the AMIS plant is mixed with the air stream entering the towers and then processed by the various cells. The decision to divide the emissions of the process into two gas outputs is made to better simulate the measurement conditions reported by EGP: as a matter of fact, the aforementioned gaseous stream leaving the AMIS is sent to two plant cells; the Hg concentration emitted by the towers is measured on the third cell to which the gas coming from the AMIS system is not supplied. This concentration is then multiplied by the total flow exiting the towers, thus obtaining the total mass rate of emitted Hg. With the aim of representing the simulated three-cell system by a single absorption tower, it has been decided to keep the stream coming from the AMIS physically separate from air inflow in the tower. Finally, as a conservative choice, the simulation model has been calibrated so that the quantity of Hg re-injected is practically zero. This arrangement is conservative because all the mercury entering the system through the turbine and not abated by the AMIS system leaves the evaporative tower, maximizing the emission.

4.2. Choice and refinement of the thermodynamic correlation

For the construction of a simulation model, the choice of a proper thermodynamic correlation is a fundamental step in order to obtain simulation results that are sufficiently representative of the real operating conditions of the process. In general, this choice is determined by the several factors: stream compositions, operating conditions (temperature and pressure), and unit operations of the process. Considering the geothermal fluid sent to the turbine and the various process streams composed mainly of water and a noncondensable gas fraction, as well as the operating conditions that see a strong variability of the pressure (from 20 bara to 0.08 bara) and temperature (from over 200 °C to 25 °C), the choice falls back to an Equation of State (EOS) model. Given the operating conditions of the GTTP taken into consideration, and the fact that the interest is in modeling liquid-vapor equilibria between the main pollutants and the preponderant component (water), the chosen correlation, among all the EOS thermodynamic packages offered by UniSim Design® R440, is the Peng-Robinson. This appears to be the most complete and most validated for the interactions of all considered components, with the exception of mercury, and for all unit operations and working conditions the process. Since the model must be oriented to a (conservative) estimate of mercury emissions, the thermodynamic correlation must be refined so that it adequately manages the liquid/vapor balance of the component of interest.

4.2.1. Liquid/vapor equilibrium related to mercury (Hg)

Given the compositions involved in the main streams, it appears that the component in the largest amount is water and consequently the most relevant interaction for this analysis is H_2O-Hg. The mixture H_2O-Hg is highly

Table 2: Values of k_{ij} found interpolating the literature data present in [32].

T(°C)	$\mathscr{H}_{\mathbf{Hg}}$**[atm]**	$\mathbf{k_{ij}}$
20	246	0.6075
25	482	0.6393
30	658	0.6537
35	878	0.6675
40	1150	0.6812

non-ideal, and experimental data retrieved at the operating conditions of the various unit operations would be needed to obtain a more reliable interaction model. Unfortunately, the simulation software used does not have a specific thermodynamic package suitable for this mixture. The Peng-Robinson correlation expresses the balance between the various components of a mixture through the following relation:

$$P = \frac{RT}{(V-b)} - \frac{a}{(V(V+b)+b(V-b))} \tag{1}$$

where

$$a = \sum_{i=1}^{N}\sum_{j=1}^{N} x_i x_j (a_i a_j)^{0.5}(1-k_{ij}) \tag{2}$$

in which

$$k_{ij} = A_{ij} + B_{ij}T + C_{ij}T^2 + \exp\left(D_{ij} + \frac{E_{ij}}{T}\right) \tag{3}$$

The terms b, a_i, a_j refer to the critical thermodynamic quantities of the individual substances of the mixture. For those components for which the interaction is not known, the value of $k_{ij} = 0$, which means, as can be deduced from the above equations, that the mutual interaction of these two species is considered ideal. In order to find the correct value of k_{ij}, relative to the H_2O-Hg pair, a literature search has been conducted concerning Henry's constant for equilibrium $Hg_{(g)} \leftrightarrow Hg_{(aq)}$. The experiments proposed in literature have been reproduced in the simulator and the k_{ij} values has been modified such that the constants calculated at the various temperatures reflect the data found. In order to find the value of A_{ij} and B_{ij} coefficients to be used in the model, a linear least-squares interpolation of the data has been performed.

Glew et al. [32] have conducted experiments in helium atmosphere at constant pressure (1 atm) to measure the solubility of liquid Hg in water, studying the equilibrium $Hg_{(l)} \leftrightarrow Hg_{(aq)}$. The values of Henry's constant ($\mathscr{H}_{Hg}$) at different temperatures are also provided: the constant is calculated as the ratio of the saturation pressure of Hg (p^0_{Hg}) at that temperature and its corresponding molar fraction in the liquid phase (x_{Hg}). In the simulation model the constant $\mathscr{H}^*_{Hg} = \frac{y_{Hg}}{x_{Hg}}$ has been calculated, where y_{Hg} is the molar fraction of Hg contained in the gaseous phase. As a matter of fact, since the total pressure of the experiment is maintained at the value of 1 atm, the correspondence $\mathscr{H}_{Hg} = \mathscr{H}^*_{Hg}$ holds true since, for the considered concentration values and the equilibrium established, the relation $p^0_{Hg} = y_{Hg}P_{tot}$ is verified. Values provided by the literature and the corresponding k_{ij} are shown in Table 2.

Sanemasa [33], instead, conducted a vacuum experiment to measure the solubility of the Hg steam in water, providing values of Henry's constant and a relation to calculate its value for the non-tabulated temperatures in the experiment. The constant is calculated as the ratio of the partial pressure of Hg (p_{Hg}) to that temperature and its corresponding mole fraction in the phase liquid (x_{Hg}). Being the vacuum pressure used by Sanemasa not known, the simulation has been carried out in the same way as the previous case, i.e. a constant total pressure of 1 atm in a helium atmosphere. In this way the constant $\mathscr{H}^*_{Hg} = \frac{y_{Hg}}{x_{Hg}}$ is calculated; holding the same considerations as before, $\mathscr{H}_{Hg} = \mathscr{H}^*_{Hg}P$. In order to calculate the $\mathscr{H}_{Hg}$ data at the temperatures in Table 2, the following relation is used [33]:

$$\log_{10}\mathscr{H}_{Hg} = \frac{-1078}{T} + 6.25 \tag{4}$$

where T is expressed in Kelvin.

Table 3: Values of k_{ij} found interpolating the literature data present in [33].

T(°C)	$\mathscr{H}_{Hg}$[atm]	k_{ij}
20	372.2	0.6280
25	429.0	0.6333
30	492.3	0.6385
35	562.3	0.6438
40	639.6	0.6491

Table 4: Values of k_{ij} found interpolating the literature data present in [34].

T(°C)	$\mathscr{H}^{\dagger}_{Hg}$	k_{ij}
20	0.276	0.62925
25	0.317	0.635
30	0.362	0.64075
35	0.412	0.6465
40	0.467	0.65225

Values of $\mathscr{H}_{Hg}$ calculated from (4) and the corresponding k_{ij} are listed in Table 4.

Finally, Andersson et al. [34] conducted a study specifically to calculate Henry's constant for the equilibrium $Hg_{(g)} \leftrightarrow Hg_{(aq)}$. Specifically, the authors calculated a dimensionless Henry constant defined as:

$$\mathscr{H}^{\dagger}_{Hg} = \frac{[Hg_{(g)}]}{[Hg_{(aq)}]} \tag{5}$$

where $[Hg_{(aq)}]$ is the Hg concentration in the aqueous phase expressed in ng m^{-3}, where the volume is the volume of water and $[Hg_{(g)}]$ is the Hg concentration in the gaseous phase expressed in ng m^{-3}, where the volume is the volume of gas. In order to calculate the value of this constant at the temperatures of interest, the following interpolation relationship is used [34]:

$$\ln \mathscr{H}^{\dagger}_{Hg} = \frac{-2404.3}{T} + 6.92 \tag{6}$$

To reproduce the experiment, a constant fraction of vapor equal to 5% is set and the temperature changed by recording the value of the constant $\mathscr{H}^{\dagger}_{Hg}$ calculated by the simulator. Values of $\mathscr{H}^{\dagger}_{Hg}$ calculated from (5) and the corresponding k_{ij} that interpolate them are reported in Table 4.

At the end of this analysis, a linear least squares interpolation is performed to find the dependance to the temperature that best approximate all the k_{ij} values. As depicted in Figure 3, the relationship found is as follows:

$$k_{ij} = 0.0654 + 0.0019T \tag{7}$$

which corresponds to the previously seen coefficients $A_{ij} = 0.0654$ and $B_{ij} = 0.0019$.

This allows us to compare Henry's constants calculated through the modified Peng-Robinson correlation, and those found in the literature. Figure 4 and 5 show the results obtained. The two graphs show the points processed by the literature correlations and the values calculated through the refinement of the thermodynamic model. For comparison, the resulting points are also illustrated using the standard Peng-Robison correlation: as expected, this latter provides values of Henry's constant very far from those of literature and it is therefore strongly inaccurate in the prediction of mercury liquid-vapor equilibrium.

4.2.2. Hydrogen sulfide (H_2S) liquid / vapor balance

The H_2S-H_2O interaction is already modeled by the thermodynamic package Peng-Robinson with the following coefficients for the calculation of k_{ij}:

$$A_{ij} = -0.3896 \quad B_{ij} = 1.565 \cdot 10^{-3} \quad C_{ij} = -1.142 \cdot 10^{-6} \tag{8}$$

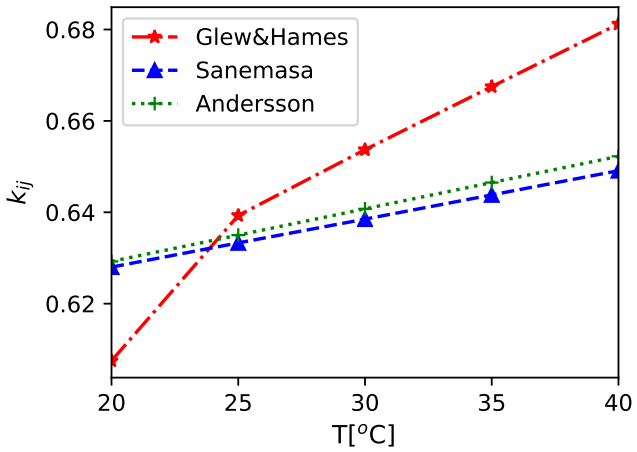

Figure 3: Linear regression of the data in the literature analyzed to find the best possible relation representing the behavior of k_{ij} with the temperature

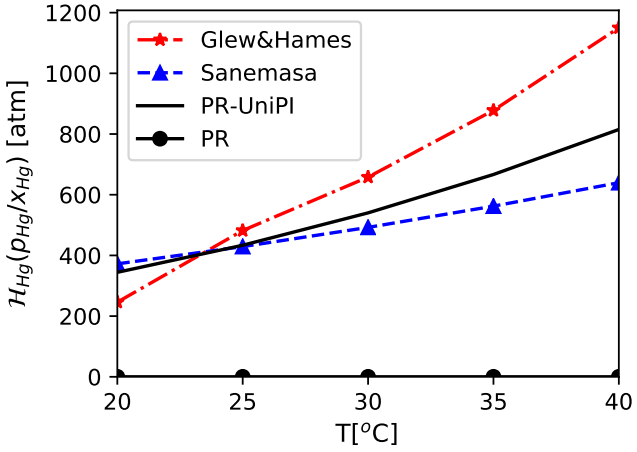

Figure 4: Comparison between literature data on the calculation of Henry's constant for the sources [32, 33]. PR-UniPI represents the modified Peng-Robinson correlation, while PR represents the standard Peng-Robinson correlation.

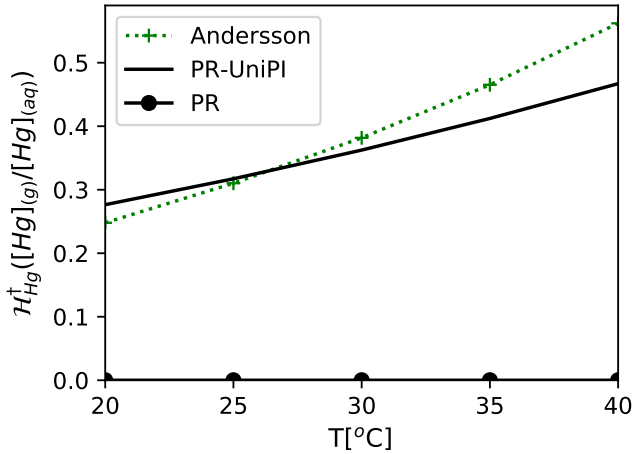

Figure 5: Comparison with literature data on the calculation of Henry's constant for the source [34]. PR-UniPI represents the modified Peng-Robinson correlation, while PR represents the standard Peng-Robinson correlation.

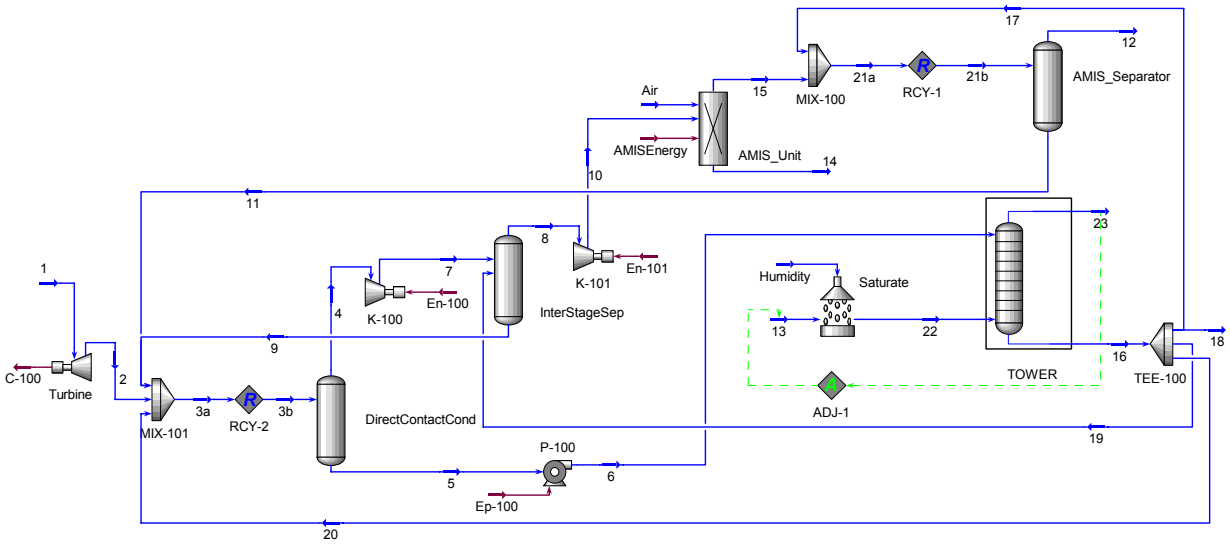

Figure 6: PFD of the geothermal power plant BG3.

A bibliographic search on some literature data [35] is carried out in order to validate the correlations available in the simulator. As explained below, this test has provided satisfactory results, and therefore an correction of thermodynamic parameters was not considered necessary. To best reproduce the experiment by Duan et al. [35] a flash separator is modeled to operate at different temperatures and test pressures. Setting an arbitrary value for the H_2S molar flow (2 kmol/h), the required water flow is calculated as follows: after the test at the temperature T_{test}, the water flow-rate F_{H_2O} is modulated so that in the gaseous stream leaving the separator the following relation holds true:

$$P_{H_2O} = P^0(T_{test}) \tag{9}$$

where P_{H_2O} is the partial pressure of water vapor, and $P^0(T)$ is the saturation pressure at the temperature T. After testing different total pressures value, it is verified how the correlation provided by the software is in full agreement with the literature data. This confirms the validity of the thermodynamic data present in the software when evaluating the H_2S-H_2O interaction.

4.3. Implementation of the simulation model

4.3.1. GTTP Bagnore 3

In this section, the development of the model of the GTPP named *Bagnore 3* (later on indicated as BG3) is described. Using UniSim Design® (version R440) and different real data sources,

The model is built on the basis of the process diagram (Figure 1) and elaborated after an accurate analysis of the technical documents made available by EGP. Comparing the BG3 model in Figure 6 with the EGP model in Figure 1, three main conceptual changes made in order to simplify its implementation have to be underlined. The first involves the condenser, which is represented by a single flash tank (in Figure 6 indicated as *DirectContactCond*), thus disregarding the temperature difference between liquid and vapor outlet streams. The second conceptual change has been applied to the section named "AMIS Unit" in Fig. 1. This is schematized with two unit operations: a component splitter (*AMIS_Unit* in Figure 6), which synthetically represents the abatement of Hg and H_2S through an efficiency taken from EGP documents [36], and a flash tank (*AMIS_Separator* in Figure 6) which separates the liquid phase from the gaseous phase coming out from the component splitter. The third and final change is about the cooling tower complex named "Cooling Tower". A single absorption column (*TOWER* in Figure 6), has been chosen as its schematization. The choice of absorption column unit operation is due to the fact that the simulation software lacks an evaporative tower model. However, being an absorption column characterized by a liquid inlet at the top and a steam

Table 5: Inputs used for the construction of the BG3 model

Stream	Parameter	Source
1	T, P, F[kg/h], composition	[36]
2	P	[37]
7	P	[37]
10	P	[36]
23	F[Nm^3/s]	[36]

Table 6: Reference and calculated quantities together with split parameter values obtained for the *CalcSplit-TEE-100* spreadsheet.

Stream	Mass Flow [kg/s]	Split value
6	1700 [37]	-
16	1700	-
17	23.3	$1.37 \cdot 10^{-2}$
18	10 [37]	$5.88 \cdot 10^{-3}$
19	111.1 [37]	$6.54 \cdot 10^{-2}$
20	1555.6 [37]	0.915

inlet at the bottom, it serves quite well the specific use. Hence, taking into consideration Figure 6, the quantities used for the construction of the model and the source from which they were taken are shown in Table 5.

Some other simplifications made during the model construction, concerning some unit operations have to be underlined. The adiabatic (or isentropic) efficiency value for the unit operation *Turbine*, is calculated in such a way that the stream *2* temperature is as close as possible to the corresponding one reported in [37], and specifically is equal to 90%. Both efficiencies of the two compressors *K-100* and *K-101* are used as optimization variables in the calibration of the model as more extensively described in Section 4.4. However, when no other information is available, for both *K-100* and *K-101*, the standard value of 80% is taken as initial value. The adiabatic efficiency of the handling pump *P-100*, has been left as default in the software and equal to 75% because no specific information about the temperature of the streams *5* and *6* was available.

Within the unit operation *AMIS_Unit* two split parameters are set to characterize the output stream *14*. For the mercury, an abatement equal to 83.1% is set, while for the hydrogen sulphide this value is 99.9%; both percentages are in mass with respect to stream *10*, the input of the *component splitter*. Both efficiency values are taken from the document [36].

For compliance with [37], a new air flow (named *Air* in Figure 6) is introduced in input to the *AMIS_Unit* and whose mass flow-rate is taken from the aforementioned document. Lacking information on operating conditions, temperature, pressure and relative humidity, the following default values have been set: 20 °C, 101.3 kPa, and 0% relative humidity.

The split values of *TEE-100* are computed using a spreadsheet operation in which the mass fractions of the various streams exiting the splitter are calculated as follows. The mass flow-rates of the streams *18, 19, 20* are taken from [37], which however does not report that of stream *17*. From measured values [37], it is observed that the difference in mass flow-rate between stream *23* and *22* is relatively small, and thus it is assumed that the liquid stream leaving the tower (*16* in Figure 6) has approximately the same mass flow as the inlet one. Hence, the mass flow-rate of stream *17* is calculated by subtracting those of streams *18, 19, 20* from the approximated rate of stream *16*, and consequently the split ratios for each stream are evaluated, as shown in Table 6. Nonetheless, it has to be noted that these splitting values are used as initial reference values for the data reconciliation procedure.

Finally, it is also necessary to underline that two logic unit operations have been included in the model. The first one is the unit operation *Adjust* (ADJ-1 in Figure 6) which is used to set (indirectly) the volumetric flow-rate of *23* to a setpoint value by varying the mass flow-rate of the air stream entering the evaporative tower (named *13* in Figure 6). The setpoint value at which the volumetric flow-rate of *23* must go is 1005 Nm^3/s [36]. The dry air stream *13* goes to the unit operation *Saturate*, from which it exits as stream *22* with a prescribed relative humidity by adding a

fictitious stream of water named *Humidity*. The relative humidity and air temperature ranges refer to those used in the Technical Report [38]. The second logic unit operation used is *Recycle* (RCY-1 and RCY-2 in Figure 6). RCY-1 is at the input to the *AMIS_Separator*, while RCY-2 is at the input to the direct-contact condenser. The decision to put the two recycling blocks at the entrance of these two unit operations, and thus create two fictitious mixtures, is purely linked to the efficiency of the simulation model. The only function of these blocks is to allow the simulator to perform cyclic calculations.

4.3.2. GTPP Nuova Radicondoli

The implementation of GTPP Nuova Radicondoli (later on indicated as RAD) model is similar to the case of Bagnore 3 one, hence for the denomination of the streams we can refer to the PFD to Figure 6. Obviously, since this is a 40MW size GTPP, the flow-rates change compared to the previous case, but also the geothermal fluid has rather different characteristics.

4.4. Data reconciliation

n the calibration of the model, with the aim of reconciling the data available, the following optimization variables were used:

- N_S: number of *TOWER* stages
- η_S: *TOWER* stage efficiency
- T_{13}: stream *13* temperature
- U_{13}: stream *13* humidity
- T_{15}: stream *15* temperature
- η_K: *K-100* and *K-101* efficiencies, gas extractor compression stages
- ξ_{TEE}: split *TEE-100* multiplier parameters

The meaning of the $\xi_{TEE,i}$ values is to multiply the mass fraction of the i-th stream (w_i), obtained from Table 6 and from the procedure explained above. The new values $w_i^{'}$ are summed among them and from these the new mass fractions $w_{TEE,i}$ used in *TEE-100* are calculated. In a compact way it can be written as follows:

$$w_i \text{ from Table 6} \rightarrow w_i^{'} = w_i \xi_{TEE,i} \rightarrow w_{TEE,i} = \frac{w_i^{'}}{\sum w_i^{'}}. \tag{10}$$

First of all, an objective function Φ is defined to account for the error between measured and model values of the following quantities: temperature of streams *6, 7, 10, 16*, mass flow-rate of streams *6, 10, 18, 19, 20*, mercury mass flow-rate of streams *10, 12, 18, 23*. The various terms of the objective function have all been normalized in the following way:

$$\Phi = \sum_{i=1}^{13} \left| \frac{\phi_i - \bar{\phi}_i}{\bar{\phi}_i} \right| \tag{11}$$

where ϕ_i indicates the value of the i-th quantity while $\bar{\phi}_i$ is its reference value (found in [36] and [37]).

Once the objective function is defined, given the integer nature of the N_S variable, the following optimization problem is defined:

$$\text{for } N_S = 1,2,3,4,5 \quad \begin{cases} \min_x \Phi(x) \\ \text{subject to} \\ x_{\min} \leq x \leq x_{\max} \end{cases} \tag{12}$$

where $x = [\eta_S; T_{13}; U_{13}; T_{15}; \eta_K; \xi_{TEE}]$. The bound constraints values for the optimization variable x are listed in Table 7.

In order to solve the optimization problem (12), the *Optimizer* tool available in UniSim Design is used. This requires the definition of a utility named *Derivative Utility* on which all the parameters, the boundary and process constraints, shown above are set. The optimizer implements a Sequential Quadratic Programming (SQP) algorithm [39], which provides a local minimum of the problem as a solution by performing a non-linear optimization.

Table 7: Bound constraints used for the data reconciliation variables

	$\mathbf{x}_{\min}$	$\mathbf{x}_{\max}$
η_S [%]	5	100
T_{13}[°C]	20	30
U_{13}[%]	50	100
T_{15}[°C]	25	45
η_K [%]	60	75
ξ_{TEE}	0.1	10

Table 8: Values of optimization variable and objective function before and after data reconciliation (BG3 case)

Quantity	**Initial value**	**Final value**
Φ	6.652	2.827
η_S [%]	65	79.5
T_{13}[°C]	28	30
U_{13}[%]	75	50.3
T_{15}[°C]	27	27.6
η_{K-100} [%]	80	70
η_{K-101} [%]	80	75
$\xi_{TEE,17}$	1	9.99
$\xi_{TEE,20}$	1	0.77
$\xi_{TEE,18}$	1	1.07
N_S	5	2

5. Results

5.1. GTPP Bagnore 3

Numerous tests have been carried out by varying the starting point of the iterations in order to get closer and closer to a global minimum. It has also to be noted how the non-linearity of the problem and the complexity of the simulation model entail a considerable computational cost. The results obtained with this procedure led to the values reported in Table 8.

The values shown in Table 9 are the best ones obtained, both for the objective function value and as a conservative model that estimates Hg emissions. Both the gaseous Hg flow-rates (streams *23* and *12*) result to be higher than their target values, albeit comparable to them as order of magnitude. As can be observed in Table 9, the Hg emissions exceed of the 56% and of the 12% their target, while Hg is practically absent in the liquid to the reinjection well. This denotes precisely the conservative nature of the model. Table 9 also shows how H_2S emission from the tower is slightly underestimated. In any case, a 19% of difference in the calculated value is considered satisfactory taking into account that in the model only physical absorption/desorption of the substances are considered, thus disregarding the chemical equilibria that in the case of H_2S plays an important role. It should also be remarked that this GTPP model has been calibrated to conservatively estimate the Hg emissions.

For completeness, the Heat and Material Balance for the BG3 model is provided in Appendix A.

5.2. GTPP Nuova Radicondoli

In the case of RAD model, the data reconciliation provided more accurate results, in terms of objective function value, than in the BG3 case. However, as can be seen from Table 10, the goal is always maintaining the conservative nature of the model. Therefore, both the output from the cooling tower and the output from the AMIS® system have a higher value than the corresponding target. The temperatures of hot (stream *5*) and cold water (stream *16*) are a little lower than reference ones: this can be explained with the hot water flow entering the cooling tower being a little higher than the target value, and this can mitigate its excessive heating inside the mixing condenser. As for the BG3

Table 9: Values of Hg and H_2S mass flows after data reconciliation for BG3 model

Quantity	**Initial**	**Final**	**Target**	Δ [%]
$F_{Hg,23}$ [g/h]	2.48	1.42	0.91	56
$F_{Hg,12}$ [g/h]	$2.97 \cdot 10^{-3}$	1.89	1.69	12
$F_{Hg,18}$ [g/h]	13.03	$1.92 \cdot 10^{-7}$	4.96	-100
$F_{H_2S,23}$ [kg/h]	15.94	9.776	12.05	-19
$F_{H_2S,12}$ [kg/h]	0.111	0.097	< 0.01	870
$F_{H_2S,18}$ [kg/h]	115	121.1	114.9	5

Table 10: Values of Hg and H_2S mass flows after data reconciliation for RAD model

Quantity	**Final**	**Target**	Δ [%]
$F_{Hg,23}$ [g/h]	1.30	1.27	2
$F_{Hg,12}$ [g/h]	0.083	0.064	30
$F_{Hg,18}$ [g/h]	9.83	8.66	14
$F_{H_2S,23}$ [kg/h]	21.128	28.9	-27
$F_{H_2S,12}$ [kg/h]	0.190	0.878	-78
$F_{H_2S,18}$ [kg/h]	211.1	191.3	10

case, Table 10 reports the Hg and H_2S flow-rates at the available measuring points. It has to noted how even in this case H_2S flow-rates are slightly lower than the target ones: this can be explained by the fact that the H_2S flow-rate entering the AMIS® system (stream *10*) is higher than the target one, and, hence much more is cut down in this section rather than being emitted from the cooling tower.

Also for the RAD model, the Heat and Material Balances can be found in Appendix B.

6. Performance analysis

6.1. Rationale

As already underlined, the major scope of the developed model is to give a conservative estimate of Hg emissions. Nonetheless, it is also important to analyze how the GTTP performance in terms of energy consumption and pollutants emission, vary according to conditions change. Hence, sensitivity analysis has been performed in order to assess how Hg and H_2S emissions along with energy consumptions/production change according to the variation of selected parameters. For the sake of brevity, only the case for BG3 is detailed, even if an identical analysis was performed for the RAD model.

Since the conditions of the geothermic fluid are quite constant over the year for a given extraction well, the parameters chosen for the sensitivity analysis are the ones most affected by seasons cycle. Hence, the most relevant variables are: temperature (T_{13}) and humidity (U_{13}) of the air used into the cooling tower, volumetric flow exiting the tower (F_{23}). These variables have a particular importance in governing the operating conditions of the condenser, together with the turbine exhaust pressure (P_2). Anyway, in order to comply more accurately with the seasonal dependence of some of these quantities, it has been decided to group some of them in three sets that represent the main seasons: summer, winter, autumn / spring. The sensitivity analysis is constructed therefore parameterizing the variation of the volumetric air flow according to these sets of environmental conditions reported in Table 11.

A consideration must be stated regarding the condenser pressure (P_2 referring to Figure 6). This quantity has been considered directly dependent on the atmospheric conditions, since, at steady state, no other control methods of this variable inside the geothermal plant are available. As a matter of fact, both air fans and gas extractor always work at constant revolutions and, therefore, the condenser pressure cannot be kept constant in all conditions. It is therefore correct to include P_2 in the seasonal sets as shown in in Table 11.

Table 11: The three sets of environmental conditions used in the parametric sensitivity analysis

	Summer	*Autumn*	*Winter*
$T_{13}[\,^{\circ}\mathrm{C}]$	28	16	8
$U_{13}[\%]$	70	75	80
P_2 [kPa]	11	9.5	8.0

Table 12: Values of power production from turbine *C-100* for the three sets of environmental conditions used in the parametric sensitivity analysis.

	Summer	*Autumn*	*Winter*
$\mathrm{Pow}_{C\text{-}100}$ [MW]	20.29	20.73	21.23

Power consumptions of the two compressors and of the pump (*En-100*, *En-101*, and *Ep-100*, respectively) are considered in the analysis. The turbine production *C-100* in the developed simulation model, depends on two parameters: the turbine efficiency and the downstream pressure (P_2). Hence, among the parameters in Table 11, the only one to affect the power generation in the turbine, is P_2. This means that for each sets in Table 11 ,a fixed value of the power production can be easily obtained from the model. Therefore, for the three ambient conditions sets, the turbine power production is reported in Table 12.

The power consumption of the tower fans, cannot be taken from the simulation, since as explained in Section 4.1, the evaporative tower has been modeled with an absorption tower. Hence, another procedure and conservative considerations have been applied. From data available in [37], the consumed power profile of the fans registered over the years seems to be more or less steady with the variation of the air flow in Nm^3/s. The maximum variation around the mean value of consumption is few percentage points. Hence, since a direct correlation between season and data could not be found, a conservative constant value has been imposed. In particular, each of the three fans, with rated power of 150 kW, is considered to consume 120 kW independently on the seasonal atmospheric conditions.

The stream *AMISEnergy* has not been considered for this analysis since it is a fictitious stream that represents different energy contributions in the AMIS® system functioning, such as heat recovery units and thermal power produced by the exothermic reactions. Its power value in the developed model, mainly depends on the temperature of the stream *15*, used as a reconciliation variable as shown in section 4.4.

6.2. Results analysis

The variation of air flow, as explained above, depends only on the weather conditions, and values between 833 and 1389 Nm^3/s at the tower exit that have been recorded in [37]. Hence, given these considerations, the variation of Hg and H_2S emissions and the energy consumption are reported in Figures 7, 8, and 9.

From Figures 7 and 8, it can be noted that the most critical environmental condition for the emissions is *Winter*. It can be seen how the increase of the ambient temperature (from *Winter* to *Summer*) leads to and increase of emissions from the AMIS® system and a reduction in the ones from the towers. This can be explained in the following way: the lower is the temperature at the condenser (*DirectContactCond* in Figure 6), the greater is the concentration of pollutants that remains in the liquid phase. As the concentration of pollutants (Hg and H_2S) in the stream directed to the evaporative towers (*5* in Figure 6) increases, the quantity treated and abated by the AMIS® system is reduced. Once arrived at the tower, most of Hg and H_2S in the liquid phase go in the gaseous phase, leading to higher values of emissions. It can be seen in Figure 8 how H_2S emissions are very sensitive to changes in ambient conditions arriving in the worst case to a difference of almost 100% between *Winter* and *Summer*.

Figure 9 confirms what already said for the pollutants emission. When the temperature of the condenser is lower, the flow to be pumped to the tower, and so the required power by *P-100*, is higher (200 kW$\rightarrow$ 300 kW). The pump power consumption is not strongly affected by the air flow variation, because varying the air flow in tower leads also to a relevant change in the condenser temperature but almost a negligible change of volumetric flow fo the liquid, so that the maximum power variation is of 30 kW (15%).

It can be also noted how in *Summer* conditions power consumed by compressor *K-101* is about 23% higher than the *Winter* case. This is explained by the fact that with higher temperature of the "cold" water coming from the tower

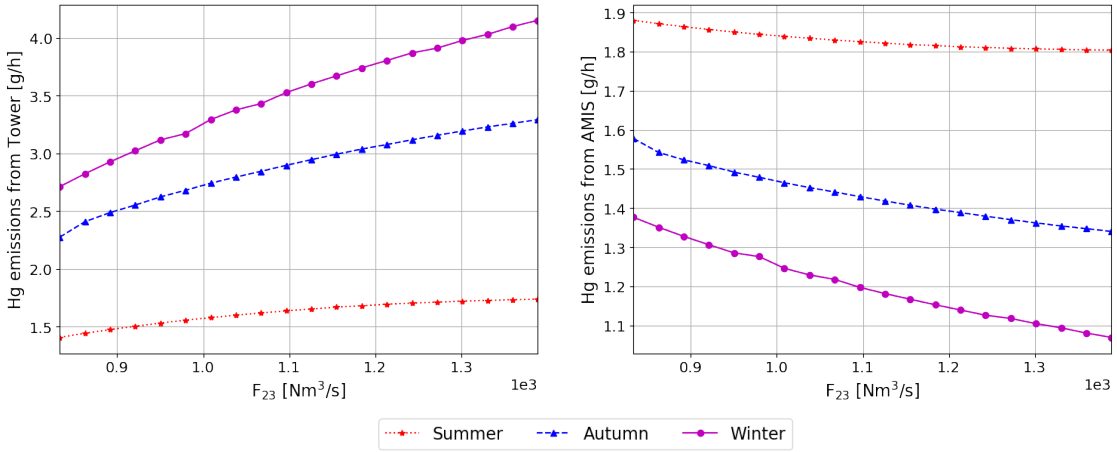

Figure 7: Hg emissions from the evaporative tower (on the left) and the AMIS® system (on the right) for different environmental conditions with the variation of the air flow exiting the towers.

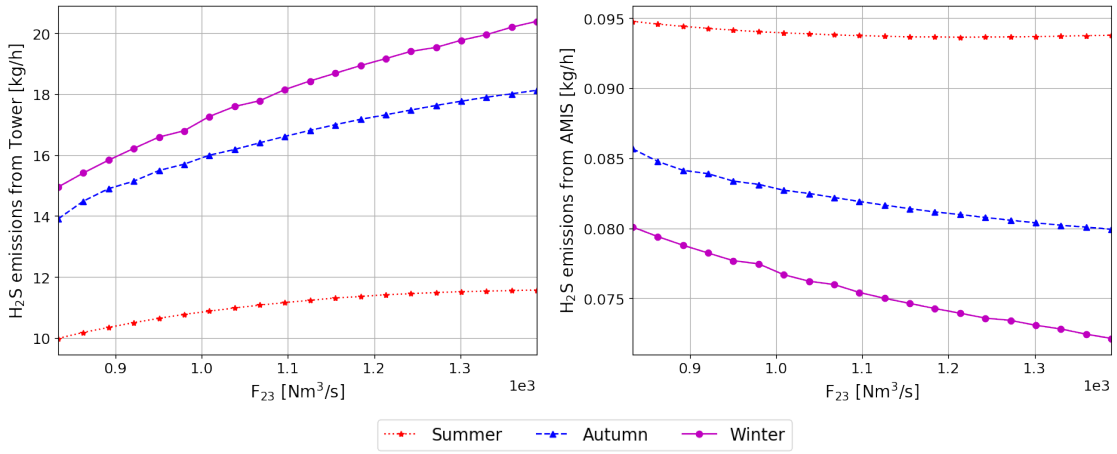

Figure 8: H_2S emissions from the evaporative tower (on the left) and the AMIS® system (on the right) for different environmental conditions with the variation of the air flow exiting the towers.

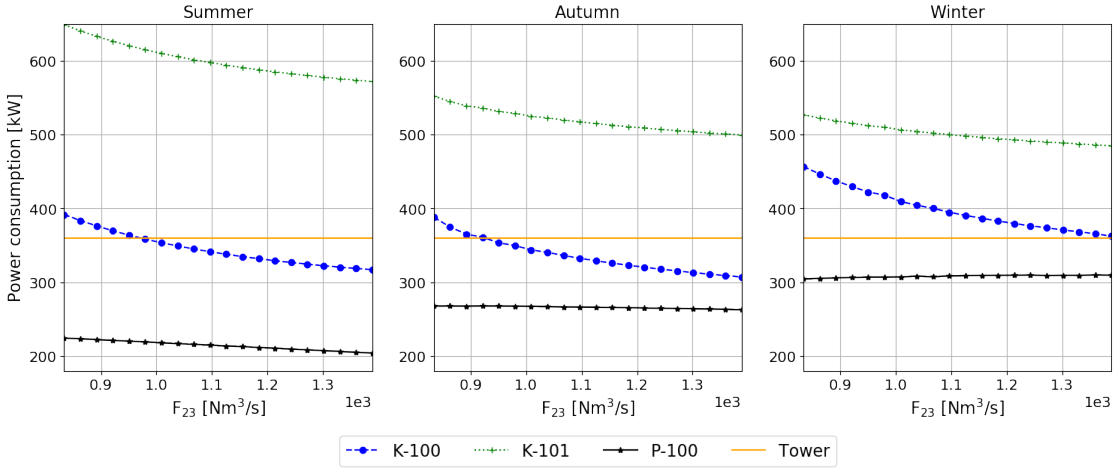

Figure 9: Energy consumption in terms of power consumed by the two compressors *K-100* and *K-101*, the pump *P-100*, and the three fans on the evaporative tower for different environmental conditions (*Summer* on the left, *Autumn* in the middle, *Winter* on the right) with the variation of the air flow exiting the towers.

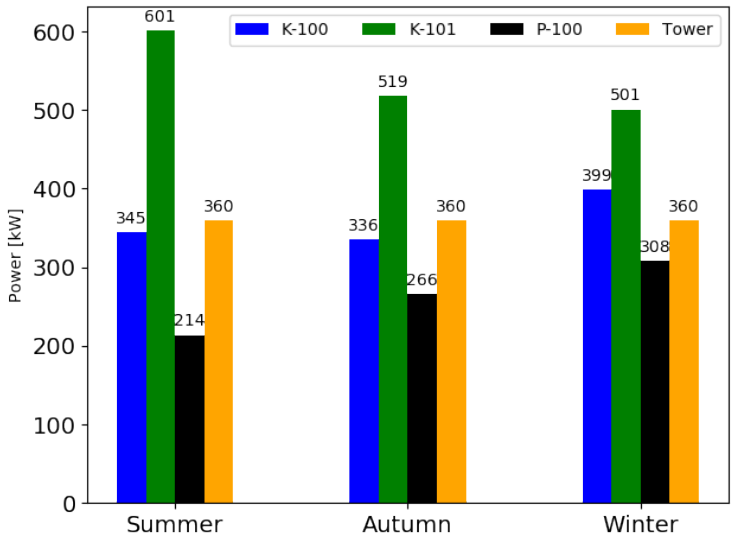

Figure 10: Mean power consumption for the two compressors *K-100* and *K-101*, the pump *P-100*, and the three fans on the evaporative tower for different environmental conditions (*Summer* on the left, *Autumn* in the middle, *Winter* on the right).

Table 13: Worst case scenarios in terms of energy consumption and emissions for different environmental conditions.

	Summer		*Autumn*		*Winter*	
F_{23} [Nm^3/s]	833	1389	833	1389	833	1389
Pow$_{C\text{-}100}$ [MW]	20.29	20.29	20.73	20.73	21.23	21.23
Pow$_{P\text{-}100}$ [MW]	0.22	0.20	0.27	0.26	0.30	0.31
Pow$_{K\text{-}100}$ [MW]	0.39	0.32	0.38	0.31	0.46	0.36
Pow$_{K\text{-}101}$ [MW]	0.65	0.57	0.55	0.50	0.53	0.48
Pow$_{Tower}$ [MW]	0.36	0.36	0.36	0.36	0.36	0.36
Net power [MW]	18.67	18.84	19.16	19.30	19.59	19.72
$F_{\text{Hg},23} + F_{\text{Hg},12}$ [g/h]	3.29	3.54	3.90	4.63	4.09	5.22
$F_{\text{H}_2\text{S},23} + F_{\text{H}_2\text{S},12}$ [kg/h]	10.07	11.66	14.30	18.20	15.03	20.46

(*9* in Figure 6), the working temperature of the intercooler is higher. For this reason the volumetric flow of *8* to be compressed in *K-101* is higher and so its consumed power.

Compressor *K-100* has a maximum consumption of 400 kW and a minimum of 300 kW in both *Summer* and *Autumn*, but a higher profile of power (about $\approx +12\%$) during the *Winter*. This can be explained in the following way: since a much higher value of recirculated mass of liquid is obtained in the *Winter* case, a higher volume of gases leaves the condenser to be compressed. At the same time, the lower temperature in the intercooler makes most of the aqueous vapor to condense so that the volumetric flow to *K-101* is much less.

Finally, as the tower fan consumption has been considered constant, it can be seen how in *Summer* and *Autumn* conditions 360 kW exceeds *P-100* consumption and most of *K-100* one. In the *Winter* conditions, instead, the contribution of the tower fan power to net one is lower in percentage than the compressors.

With these considerations, Figure 10 shows the mean power contributions to the total power consumption for each season condition, summarizing what already discussed above. Finally, considering also the turbine power generation in Table 12, the worst case scenarios in terms of energy consumptions can be easily calculated. Together with the pollutant emissions, the produced net power, corresponding to these scenarios, is reported in Table 13.

From this analysis, it follows that the energetic performances of the GTPP are mostly affected by ambient conditions rather than from the effort required to stay within the emission limit values and achieve environmental performances.

7. Conclusion

Geothermal power plants (GTPPs) are well established solutions to produce electrical power from a green source. Exploiting a hot fluid trapped under rock layers at high pressures, many substances present in the soil of the well area are transported with it. In Italy, specifically in Tuscany, there is the largest geothermal energy area of the world. Unfortunately, the soil is also rich in heavy metals and especially in mercury that is emitted from GTPPs together with other pollutants. Since determining on-line the mass flow of mercury exiting the evaporative towers of a GTPP plant is a difficult simple task, a detailed simulation model of the plant has been developed in UniSim Design® to follow the route of this substance from the extraction well to its emission in the atmosphere and to analyze also the pollutant distribution among the various unit operations as the operating and process conditions change.

The various modeling phases have been described, underling assumptions and issues faced during the simulation. The model has been developed from real data and a reconciliation procedure via optimization has been conducted. Satisfactory results obtained for the modeling of two different real plants of 20 MWe and 40 MWe of nominal power, respectively, have been illustrated. In both cases mercury emissions have been slightly overestimated due to the (intended) conservative nature of the GTPP model. The deviation obtained is 27% over the target value for the first plant, that is 3.31 g/h calculated against 2.6 g/h measured, and 4% for the second one, that is 1.38 g/h calculated against 1.33 g/h measured. On the other hand, emissions of the hydrogen sulfide are underestimated, an explainable behavior since the software does not take in consideration the chemical reactions that may occur. The maximum underestimation for the first plant is -19%, that is 16.05 kg/h calculated against 9.87 kg/h measured, while a little bit higher, -27%, for the second one, that is 21.32 kg/h calculated against 29.78 kg/h measured.

Finally a performance analysis in terms of emission and power consumptions has been performed, and for the sake of brevity only the analysis to the first plant has been shown. Net power generation has been calculated in the identified worst case scenarios for each set of the selected environmental conditions. A minimum net power generation of 18.67 MW has been found in summer conditions, while the maximum emission of pollutants is related to winter conditions (5.22 g/h of total mercury and 20.46 kg/h of hydrogen sulfide).

To conclude, this study showed that energetic performances of GTTPs are influenced by seasonal conditions and, at the same time, independent from the environmental measures adopted.

References

[1] R. Bertani, Geothermal power generation in the world 2010–2014 update report, Geothermics 60 (2016) 31–43.

[2] C. Willems, H. M. Nick, Towards optimisation of geothermal heat recovery: An example from the West Netherlands Basin, Applied Energy 247 (2019) 582 – 593.

[3] Q. Liu, L. Shang, Y. Duan, Performance analyses of a hybrid geothermal-fossil power generation system using low-enthalpy geothermal resources, Applied Energy 162 (2016) 149 – 162.

[4] A. Anderson, B. Rezaie, Geothermal technology: Trends and potential role in a sustainable future, Applied Energy 248 (2019) 18–34.

[5] P. Bayer, L. Rybach, P. Blum, R. Brauchler, Review on life cycle environmental effects of geothermal power generation, Renewable and Sustainable Energy Reviews 26 (2013) 446–463.

[6] C. Tomasini-Montenegro, E. Santoyo-Castelazo, H. Gujba, R. Romero, E. Santoyo, Life cycle assessment of geothermal power generation technologies: An updated review, Applied Thermal Engineering 114 (2017) 1119–1136.

[7] E. Bacci, C. Gaggi, E. Lanzillotti, S. Ferrozzi, L. Valli, Geothermal power plants at Mt. Amiata (Tuscany-Italy): mercury and hydrogen sulphide deposition revealed by vegetation, Chemosphere 40 (8) (2000) 907 – 911.

[8] S. Loppi, Environmental distribution of mercury and other trace elements in the geothermal area of Bagnore (Mt. Amiata, Italy), Chemosphere 45 (6-7) (2001) 991–995.

[9] M. L. Parisi, N. Ferrara, L. Torsello, R. Basosi, Life cycle assessment of atmospheric emission profiles of the italian geothermal power plants, Journal of Cleaner Production.

[10] A. Manzella, R. Bonciani, A. Allansdottir, S. Botteghi, A. Donato, S. Giamberini, A. Lenzi, M. Paci, A. Pellizzone, D. Scrocca, Environmental and social aspects of geothermal energy in Italy, Geothermics 72 (2018) 232–248.

[11] J. Cabassi, F. Tassi, S. Venturi, S. Calabrese, F. Capecchiacci, W. D'Alessandro, O. Vaselli, A new approach for the measurement of gaseous elemental mercury (GEM) and H_2S in air from anthropogenic and natural sources: Examples from Mt. Amiata (Siena, Central Italy) and Solfatara Crater (Campi Flegrei, Southern Italy), Journal of geochemical exploration 175 (2017) 48–58.

[12] UNI EN, UNI EN 13211:2003 (2003).

[13] A. Lenzi, A. Caprai, A. D'Ulivo, M. Onor, M. Mascherpa, M. Paci, R. Taccone, A. Bettini, A. Ciompi, Sampling and analysis procedure for the determination of mercury leaving cooling towers in geothermal power stations IGG-ICCOM/CNR-3 METHOD (M3). In collaboration with ARPAT-geothermal sector, ARPAT laboratory sector AVS siena 3 IGG/CNR-3 METHOD 2 CONTENTS (09 2017).

[14] US EPA, US E.P.A METHOD 29, Determination of Metals Emissions from Stationary Sources (2017).

[15] Y. Cerci, Performance evaluation of a single-flash geothermal power plant in Denizli, Turkey, Energy 28 (1) (2003) 27–35.

[16] S. Jalilinasrabady, R. Itoi, P. Valdimarsson, G. Saevarsdottir, H. Fujii, Flash cycle optimization of Sabalan geothermal power plant employing exergy concept, Geothermics 43 (2012) 75–82.
[17] C. Coskun, Z. Oktay, I. Dincer, Performance evaluations of a geothermal power plant, Applied Thermal Engineering 31 (17-18) (2011) 4074–4082.
[18] M. Kanoglu, Exergy analysis of a dual-level binary geothermal power plant, Geothermics 31 (6) (2002) 709–724.
[19] M. Unverdi, Y. Cerci, Performance analysis of Germencik geothermal power plant, Energy 52 (2013) 192–200.
[20] J.-A. R. Sarr, F. Mathieu-Potvin, Improvement of Double-Flash geothermal power plant design: A comparison of six interstage heating processes, Geothermics 54 (2015) 82–95.
[21] N. A. Pambudi, R. Itoi, S. Jalilinasrabady, K. Jaelani, Performance improvement of a single-flash geothermal power plant in Dieng, Indonesia, upon conversion to a double-flash system using thermodynamic analysis, Renewable energy 80 (2015) 424–431.
[22] O. Arslan, O. Yetik, ANN based optimization of supercritical ORC-Binary geothermal power plant: Simav case study, Applied Thermal Engineering 31 (17-18) (2011) 3922–3928.
[23] Y. Zhao, J. Wang, Exergoeconomic analysis and optimization of a flash-binary geothermal power system, Applied energy 179 (2016) 159–170.
[24] A. Aali, N. Pourmahmoud, V. Zare, Exergoeconomic analysis and multi-objective optimization of a novel combined flash-binary cycle for Sabalan geothermal power plant in iran, Energy Conversion and Management 143 (2017) 377–390.
[25] M.-R. Kolahi, A. Nemati, M. Yari, Performance optimization and improvement of a flash-binary geothermal power plant using zeotropic mixtures with PSO algorithm, Geothermics 74 (2018) 45–56.
[26] A. Mosaffa, A. Zareei, Proposal and thermoeconomic analysis of geothermal flash binary power plants utilizing different types of organic flash cycle, Geothermics 72 (2018) 47–63.
[27] N. A. Pambudi, R. Itoi, S. Jalilinasrabady, M. Gürtürk, Sustainability of geothermal power plant combined with thermodynamic and silica scaling model, Geothermics 71 (2018) 108–117.
[28] J. Zhu, K. Hu, W. Zhang, X. Lu, A study on generating a map for selection of optimum power generation cycles used for Enhanced Geothermal Systems, Energy 133 (2017) 502–512.
[29] M. Yari, Exergetic analysis of various types of geothermal power plants, Renewable energy 35 (1) (2010) 112–121.
[30] I. Lee, J. W. Tester, F. You, Systems analysis, design, and optimization of geothermal energy systems for power production and polygeneration: State-of-the-art and future challenges, Renewable and Sustainable Energy Reviews 109 (2019) 551–577.
[31] A. Baldacci, M. Mannari, F. Sansone, Greening of geothermal power: an innovative technology for abatement of hydrogen sulphide and mercury emission, in: Proceedings of the World Geothermal Congress, Antalya, Turkey, Vol. 2429, 2005.
[32] D. Glew, D. Hames, Aqueous nonelectrolyte solutions. Part X. mercury solubility in water, Canadian Journal of Chemistry 49 (19) (1971) 3114–3118.
[33] I. Sanemasa, The solubility of elemental mercury vapor in water, Bulletin of the Chemical Society of Japan 48 (6) (1975) 1795–1798.
[34] M. E. Andersson, K. Gårdfeldt, I. Wängberg, D. Strömberg, Determination of Henry's law constant for elemental mercury, Chemosphere 73 (4) (2008) 587–592.
[35] Z. Duan, R. Sun, R. Liu, C. Zhu, Accurate thermodynamic model for the calculation of H_2S solubility in pure water and brines, Energy & Fuels 21 (4) (2007) 2056–2065.
[36] M. Paci, R. Bonciani, Personal communication: Data on AMIS® performance monitoring campaign (July 2014).
[37] M. Paci, R. Bonciani, Personal communication: Data for GTPP of 20MW (July 2014).
[38] M. Paci, V. Nardi, Messa a punto di un metodo indiretto per la valutazione delle emissioni di mercurio dalle torri evaporative di centrali geotermoelettriche (2014).
[39] J. Nocedal, S. J. Wright, Numerical optimization 2nd, Springer, 2006.

Appendix A. Heat and material balance sheet for BG3 model

The Heat and Material Balance for the BG3 model is provided in Table A.15, while energy streams values are listed in Table A.14.

Table A.14: Energy streams for BG3 model.

Stream	*C-100*	*En-100*	*En-101*
Heat Flow [kW]	$2.094 \cdot 10^4$	$3.484 \cdot 10^2$	$5.997 \cdot 10^2$
Stream	*Ep-100*	*AMISEnergy*	
Heat Flow [kW]	$1.913 \cdot 10^2$	$-1.568 \cdot 10^3$	

Appendix B. Heat and material balance sheet for RAD model

Table A.15: Heat and Material Balance table for BG3 model. When *Recycle* unit operation is present, only the streams denoted with "*a*" are listed.

Stream	*1*	*2*	*3a*	*4*	*5*	*7*	*8*	*9*	*10*	*12*	*11*	*23*	*13*
Mass Flow [kg/s]	$3.494{\cdot}10^{1}$	$3.494{\cdot}10^{1}$	$1.590{\cdot}10^{3}$	4.208	$1.586{\cdot}10^{3}$	4.208	3.163	$1.133{\cdot}10^{2}$	3.163	2.834	$2.362{\cdot}10^{2}$	$1.271{\cdot}10^{2}$	$1.234{\cdot}10^{3}$
Temperature [°C]	210.80	46.84	36.56	36.56	36.56	101.65	34.36	34.36	205.38	28.46	28.46	32.46	30.00
Pressure [kPa]	2020	11	11	11	11	20	20	20	101.5	100	100	100	110
Molecular Weight	18.80	18.80	18.03	28.46	18.02	28.46	35.04	18.02	35.04	38.68	18.02	28.35	28.85
Mass Density [kg/m^3]	12.78	0.11	43.97	0.12	998.51	0.18	0.27	1000.24	0.90	1.55	1004.84	1.12	1.26
Mass Enhtalpy [kJ/kg]	$-1.312{\cdot}10^{4}$	$-1.370{\cdot}10^{4}$	$-1.582{\cdot}10^{4}$	$-1.027{\cdot}10^{4}$	$-1.584{\cdot}10^{4}$	$-1.019{\cdot}10^{4}$	$-9.265{\cdot}10^{3}$	$-1.585{\cdot}10^{4}$	$-9.076{\cdot}10^{3}$	$-7.917{\cdot}10^{3}$	$-1.587{\cdot}10^{4}$	$-3.830{\cdot}10^{2}$	4.756
H_2O Mass Fraction	$9.239{\cdot}10^{-1}$	$9.239{\cdot}10^{-1}$	$9.981{\cdot}10^{-1}$	$3.482{\cdot}10^{-1}$	$9.999{\cdot}10^{-1}$	$3.482{\cdot}10^{-1}$	$1.379{\cdot}10^{-1}$	$9.998{\cdot}10^{-1}$	$1.379{\cdot}10^{-1}$	$1.803{\cdot}10^{-2}$	$9.991{\cdot}10^{-1}$	$2.903{\cdot}10^{-2}$	0.000
H_2S Mass Fraction	$1.041{\cdot}10^{-3}$	$1.041{\cdot}10^{-3}$	$2.324{\cdot}10^{-5}$	$8.137{\cdot}10^{-3}$	$1.712{\cdot}10^{-6}$	$8.137{\cdot}10^{-3}$	$1.064{\cdot}10^{-2}$	$5.202{\cdot}10^{-6}$	$1.064{\cdot}10^{-2}$	$9.505{\cdot}10^{-6}$	$2.844{\cdot}10^{-8}$	$2.137{\cdot}10^{-6}$	0.000
H_2 Mass Fraction	$4.213{\cdot}10^{-5}$	$4.213{\cdot}10^{-5}$	$9.261{\cdot}10^{-7}$	$3.499{\cdot}10^{-4}$	$9.272{\cdot}10^{-11}$	$3.499{\cdot}10^{-4}$	$4.656{\cdot}10^{-4}$	$2.599{\cdot}10^{-10}$	$4.656{\cdot}10^{-4}$	$5.194{\cdot}10^{-4}$	$1.358{\cdot}10^{-9}$	$1.157{\cdot}10^{-10}$	0.000
NH_3 Mass Fraction	$2.259{\cdot}10^{-3}$	$2.259{\cdot}10^{-3}$	$1.035{\cdot}10^{-4}$	$9.769{\cdot}10^{-4}$	$1.012{\cdot}10^{-4}$	$9.769{\cdot}10^{-4}$	$3.134{\cdot}10^{-4}$	$7.958{\cdot}10^{-5}$	$3.134{\cdot}10^{-4}$	$3.126{\cdot}10^{-5}$	$5.621{\cdot}10^{-5}$	$6.160{\cdot}10^{-5}$	0.000
HCl Mass Fraction	$1.198{\cdot}10^{-6}$	$1.198{\cdot}10^{-6}$	$2.774{\cdot}10^{-8}$	$1.029{\cdot}10^{-5}$	$5.113{\cdot}10^{-10}$	$1.029{\cdot}10^{-5}$	$1.364{\cdot}10^{-5}$	$1.511{\cdot}10^{-9}$	$1.364{\cdot}10^{-5}$	$1.449{\cdot}10^{-5}$	$8.759{\cdot}10^{-9}$	$6.379{\cdot}10^{-10}$	0.000
Hg Mass Fraction	$1.264{\cdot}10^{-7}$	$1.264{\cdot}10^{-7}$	$2.950{\cdot}10^{-9}$	$1.021{\cdot}10^{-6}$	$2.490{\cdot}10^{-10}$	$1.021{\cdot}10^{-6}$	$1.330{\cdot}10^{-6}$	$7.934{\cdot}10^{-10}$	$1.330{\cdot}10^{-6}$	$1.857{\cdot}10^{-7}$	$7.814{\cdot}10^{-10}$	$3.106{\cdot}10^{-10}$	0.000
CH_4 Mass Fraction	$1.948{\cdot}10^{-3}$	$1.948{\cdot}10^{-3}$	$4.280{\cdot}10^{-5}$	$1.617{\cdot}10^{-2}$	$2.993{\cdot}10^{-11}$	$1.617{\cdot}10^{-2}$	$2.152{\cdot}10^{-2}$	$7.867{\cdot}10^{-11}$	$2.152{\cdot}10^{-2}$	$2.401{\cdot}10^{-2}$	$3.437{\cdot}10^{-10}$	$3.735{\cdot}10^{-11}$	0.000
CO_2 Mass Fraction	$7.040{\cdot}10^{-2}$	$7.040{\cdot}10^{-2}$	$1.675{\cdot}10^{-3}$	$6.179{\cdot}10^{-1}$	$4.018{\cdot}10^{-5}$	$6.179{\cdot}10^{-1}$	$8.176{\cdot}10^{-1}$	$1.243{\cdot}10^{-4}$	$8.176{\cdot}10^{-1}$	$8.455{\cdot}10^{-1}$	$8.025{\cdot}10^{-4}$	$5.014{\cdot}10^{-5}$	0.000
N_2 Mass Fraction	$3.593{\cdot}10^{-4}$	$3.593{\cdot}10^{-4}$	$1.891{\cdot}10^{-5}$	$7.140{\cdot}10^{-3}$	$1.324{\cdot}10^{-8}$	$7.140{\cdot}10^{-3}$	$9.997{\cdot}10^{-3}$	$4.264{\cdot}10^{-8}$	$9.997{\cdot}10^{-3}$	$8.732{\cdot}10^{-2}$	$2.233{\cdot}10^{-6}$	$7.447{\cdot}10^{-1}$	$7.671{\cdot}10^{-1}$
O_2 Mass Fraction	$9.062{\cdot}10^{-5}$	$9.062{\cdot}10^{-5}$	$2.903{\cdot}10^{-6}$	$1.097{\cdot}10^{-3}$	$7.455{\cdot}10^{-10}$	$1.097{\cdot}10^{-3}$	$1.501{\cdot}10^{-3}$	$2.175{\cdot}10^{-9}$	$1.501{\cdot}10^{-3}$	$2.459{\cdot}10^{-2}$	$1.723{\cdot}10^{-7}$	$2.261{\cdot}10^{-1}$	$2.329{\cdot}10^{-1}$

Stream	*6*	*18*	*17*	*15*	*14*	*16*	*20*	*22*	*Humidity*	*Air*	*19*	*21a*
Mass Flow [kg/s]	$1.586{\cdot}10^{3}$	$1.084{\cdot}10^{1}$	$2.356{\cdot}10^{2}$	3.407	$3.362{\cdot}10^{-2}$	$1.564{\cdot}10^{3}$	$1.206{\cdot}10^{3}$	$1.249{\cdot}10^{3}$	$1.551{\cdot}10^{1}$	$2.778{\cdot}10^{-1}$	$1.122{\cdot}10^{2}$	$2.390{\cdot}10^{2}$
Temperature [°C]	36.57	28.39	28.39	27.64	69.60	28.39	28.39	30.00	20.00	20.00	28.39	28.46
Pressure [kPa]	101.325	100	100	101.3	120	100	100	110	100	101.325	100	100
Molecular Weight	18.02	18.02	18.02	34.44	34.08	18.02	18.02	28.64	18.02	28.85	18.02	18.14
Mass Density [kg/m^3]	998.53	1004.81	1004.81	1.79	1.44	1004.81	1004.81	1.25	1011.11	1.20	1004.81	115.78
Mass Enhtalpy [kJ/kg]	$-1.584{\cdot}10^{4}$	$-1.587{\cdot}10^{4}$	$-1.587{\cdot}10^{4}$	$-8.881{\cdot}10^{3}$	$-5.483{\cdot}10^{2}$	$-1.587{\cdot}10^{4}$	$-1.587{\cdot}10^{4}$	$-1.619{\cdot}10^{2}$	$-1.591{\cdot}10^{4}$	-5.342	$-1.587{\cdot}10^{4}$	$-1.577{\cdot}10^{4}$
H_2O Mass Fraction	$9.999{\cdot}10^{-1}$	$9.999{\cdot}10^{-1}$	$9.999{\cdot}10^{-1}$	$1.281{\cdot}10^{-1}$	0.000	$9.999{\cdot}10^{-1}$	$9.999{\cdot}10^{-1}$	$1.241{\cdot}10^{-2}$	1.000	0.000	$9.999{\cdot}10^{-1}$	$9.875{\cdot}10^{-1}$
H_2S Mass Fraction	$1.712{\cdot}10^{-6}$	$1.890{\cdot}10^{-11}$	$1.890{\cdot}10^{-11}$	$9.878{\cdot}10^{-6}$	$9.999{\cdot}10^{-1}$	$1.890{\cdot}10^{-11}$	$1.890{\cdot}10^{-11}$	0.000	0.000	0.000	$1.890{\cdot}10^{-11}$	$1.408{\cdot}10^{-7}$
H_2 Mass Fraction	$9.272{\cdot}10^{-11}$	$9.344{\cdot}10^{-22}$	$9.344{\cdot}10^{-22}$	$4.322{\cdot}10^{-4}$	0.000	$9.344{\cdot}10^{-22}$	$9.344{\cdot}10^{-22}$	0.000	0.000	0.000	$9.344{\cdot}10^{-22}$	$6.160{\cdot}10^{-6}$
NH_3 Mass Fraction	$1.012{\cdot}10^{-4}$	$5.252{\cdot}10^{-5}$	$5.252{\cdot}10^{-5}$	$2.909{\cdot}10^{-4}$	0.000	$5.252{\cdot}10^{-5}$	$5.252{\cdot}10^{-5}$	0.000	0.000	0.000	$5.252{\cdot}10^{-5}$	$5.592{\cdot}10^{-5}$
HCl Mass Fraction	$5.113{\cdot}10^{-10}$	$2.494{\cdot}10^{-16}$	$2.494{\cdot}10^{-16}$	$1.266{\cdot}10^{-5}$	0.000	$2.494{\cdot}10^{-16}$	$2.494{\cdot}10^{-16}$	0.000	0.000	0.000	$2.494{\cdot}10^{-16}$	$1.804{\cdot}10^{-7}$
Hg Mass Fraction	$2.490{\cdot}10^{-10}$	$4.934{\cdot}10^{-15}$	$4.934{\cdot}10^{-15}$	$2.087{\cdot}10^{-7}$	$1.040{\cdot}10^{-4}$	$4.934{\cdot}10^{-15}$	$4.934{\cdot}10^{-15}$	0.000	0.000	0.000	$4.934{\cdot}10^{-15}$	$2.974{\cdot}10^{-9}$
CH_4 Mass Fraction	$2.993{\cdot}10^{-11}$	$1.015{\cdot}10^{-26}$	$1.015{\cdot}10^{-26}$	$1.998{\cdot}10^{-2}$	0.000	$1.015{\cdot}10^{-26}$	$1.015{\cdot}10^{-26}$	0.000	0.000	0.000	$1.015{\cdot}10^{-26}$	$2.847{\cdot}10^{-4}$
CO_2 Mass Fraction	$4.018{\cdot}10^{-5}$	$4.411{\cdot}10^{-11}$	$4.411{\cdot}10^{-11}$	$7.590{\cdot}10^{-1}$	0.000	$4.411{\cdot}10^{-11}$	$4.411{\cdot}10^{-11}$	0.000	0.000	0.000	$4.411{\cdot}10^{-11}$	$1.082{\cdot}10^{-2}$
N_2 Mass Fraction	$1.324{\cdot}10^{-8}$	$1.408{\cdot}10^{-5}$	$1.408{\cdot}10^{-5}$	$7.182{\cdot}10^{-2}$	0.000	$1.408{\cdot}10^{-5}$	$1.408{\cdot}10^{-5}$	$7.576{\cdot}10^{-1}$	0.000	$7.671{\cdot}10^{-1}$	$1.408{\cdot}10^{-5}$	$1.038{\cdot}10^{-3}$
O_2 Mass Fraction	$7.455{\cdot}10^{-10}$	$1.168{\cdot}10^{-6}$	$1.168{\cdot}10^{-6}$	$2.038{\cdot}10^{-2}$	0.000	$1.168{\cdot}10^{-6}$	$1.168{\cdot}10^{-6}$	$2.300{\cdot}10^{-1}$	0.000	$2.329{\cdot}10^{-1}$	$1.168{\cdot}10^{-6}$	$2.917{\cdot}10^{-4}$

The Heat and Material Balance for the RAD model is reported in Table B.17, while energy streams values are listed in Table B.16.

Table B.16: Energy streams for RAD model.

Stream	*C-100*	*En-100*	*En-101*
Heat Flow [kW]	$4.501 \cdot 10^4$	$7.915 \cdot 10^2$	$1.009 \cdot 10^3$
Stream	*Ep-100*	*AMISEnergy*	
Heat Flow [kW]	$3.928 \cdot 10^2$	$-2.319 \cdot 10^3$	

Table B.17: Heat and Material Balance table for RAD model. When *Recycle* unit operation is present, only the streams denoted with "*a*" are listed.

Stream	*1*	*2*	*3a*	*4*	*5*	*7*	*8*	*9*	*10*	*12*	*11*	*23*	*13*
Mass Flow [kg/s]	$7.567 \cdot 10^{1}$	$7.567 \cdot 10^{1}$	$3.239E \cdot 10^{3}$	7.529	$3.232 \cdot 10^{3}$	7.529	6.196	$7.811 \cdot 10^{1}$	6.196	5.680	$1.608 \cdot 10^{2}$	$3.014 \cdot 10^{3}$	$2.959 \cdot 10^{3}$
Temperature [°C]	210.80	45.14	31.19	31.19	31.19	121.08	32.34	32.34	188.97	20.50	20.50	26.33	7.00
Pressure [kPa]	770	9.93	9.93	9.93	9.93	23.077	23.077	23.077	107.4	100	100	100	110
Molecular Weight	18.81	18.81	18.03	31.54	18.02	31.54	37.52	18.02	37.52	41.13	18.03	28.54	28.85
Mass Density [kg/m^3]	3.72	0.08	50.63	0.12	1002.65	0.22	0.34	1001.83	1.05	1.69	1010.92	1.15	1.36
Mass Enhtalpy [kJ/kg]	$-1.276 \cdot 10^{4}$	$-1.335 \cdot 10^{4}$	$-1.585 \cdot 10^{4}$	$-9.893 \cdot 10^{3}$	$-1.586 \cdot 10^{4}$	$-9.788 \cdot 10^{3}$	$-9.144 \cdot 10^{3}$	$-1.585 \cdot 10^{4}$	$-8.981 \cdot 10^{3}$	$-8.379 \cdot 10^{3}$	$-1.590 \cdot 10^{4}$	$-2.446 \cdot 10^{2}$	$-1.850 \cdot 10^{1}$
H_2O Mass Fraction	$9.269 \cdot 10^{-1}$	$9.269 \cdot 10^{-1}$	$9.982 \cdot 10^{-1}$	$2.574 \cdot 10^{-1}$	$9.999 \cdot 10^{-1}$	$2.574 \cdot 10^{-1}$	$9.965 \cdot 10^{-2}$	$9.998 \cdot 10^{-1}$	$9.965 \cdot 10^{-2}$	$1.051 \cdot 10^{-2}$	$9.989 \cdot 10^{-1}$	$1.826 \cdot 10^{-2}$	0.000
H_2S Mass Fraction	$8.523 \cdot 10^{-4}$	$8.523 \cdot 10^{-4}$	$2.005 \cdot 10^{-5}$	$7.849 \cdot 10^{-3}$	$1.816 \cdot 10^{-6}$	$7.849 \cdot 10^{-3}$	$9.463 \cdot 10^{-3}$	$5.923 \cdot 10^{-6}$	$9.463 \cdot 10^{-3}$	$9.338 \cdot 10^{-6}$	$3.480 \cdot 10^{-8}$	$1.947 \cdot 10^{-6}$	0.000
H_2 Mass Fraction	$3.428 \cdot 10^{-5}$	$3.428 \cdot 10^{-5}$	$8.008 \cdot 10^{-7}$	$3.445 \cdot 10^{-4}$	$7.853 \cdot 10^{-11}$	$3.445 \cdot 10^{-4}$	$4.187 \cdot 10^{-4}$	$2.728 \cdot 10^{-10}$	$4.187 \cdot 10^{-4}$	$4.567 \cdot 10^{-4}$	$1.003 \cdot 10^{-9}$	$8.421 \cdot 10^{-11}$	0.000
NH_3 Mass Fraction	$1.896 \cdot 10^{-4}$	$1.896 \cdot 10^{-4}$	$1.104 \cdot 10^{-5}$	$8.348 \cdot 10^{-5}$	$1.088 \cdot 10^{-5}$	$8.348 \cdot 10^{-5}$	$3.445 \cdot 10^{-5}$	$1.179 \cdot 10^{-5}$	$3.445 \cdot 10^{-5}$	$2.826 \cdot 10^{-6}$	$7.781 \cdot 10^{-6}$	$4.686 \cdot 10^{-6}$	0.000
HCl Mass Fraction	0.000	0.000	0.000	0.000	0.000	0.000	0.000	0.000	0.000	0.000	0.000	0.000	0.000
Hg Mass Fraction	$4.078 \cdot 10^{-8}$	$4.078 \cdot 10^{-8}$	$9.625 \cdot 10^{-10}$	$3.662 \cdot 10^{-7}$	$1.116 \cdot 10^{-10}$	$3.662 \cdot 10^{-7}$	$4.405 \cdot 10^{-7}$	$3.531 \cdot 10^{-10}$	$4.405 \cdot 10^{-7}$	$4.067 \cdot 10^{-9}$	$2.608 \cdot 10^{-11}$	$1.197 \cdot 10^{-10}$	0.000
CH_4 Mass Fraction	$4.331 \cdot 10^{-4}$	$4.331 \cdot 10^{-4}$	$1.012 \cdot 10^{-5}$	$4.353 \cdot 10^{-3}$	$5.906 \cdot 10^{-12}$	$4.353 \cdot 10^{-3}$	$5.290 \cdot 10^{-3}$	$2.124 \cdot 10^{-11}$	$5.290 \cdot 10^{-3}$	$5.770 \cdot 10^{-3}$	$5.396 \cdot 10^{-11}$	$6.334 \cdot 10^{-12}$	0.000
CO_2 Mass Fraction	$7.107 \cdot 10^{-2}$	$7.107 \cdot 10^{-2}$	$1.720 \cdot 10^{-3}$	$7.175 \cdot 10^{-1}$	$5.215 \cdot 10^{-5}$	$7.175 \cdot 10^{-1}$	$8.698 \cdot 10^{-1}$	$1.704 \cdot 10^{-4}$	$8.698 \cdot 10^{-1}$	$9.171 \cdot 10^{-1}$	$1.117 \cdot 10^{-3}$	$5.592 \cdot 10^{-5}$	0.000
N_2 Mass Fraction	$5.079 \cdot 10^{-4}$	$5.079 \cdot 10^{-4}$	$2.671 \cdot 10^{-5}$	$1.148 \cdot 10^{-2}$	$2.283 \cdot 10^{-8}$	$1.148 \cdot 10^{-2}$	$1.415 \cdot 10^{-2}$	$7.659 \cdot 10^{-8}$	$1.415 \cdot 10^{-2}$	$5.337 \cdot 10^{-2}$	$1.652 \cdot 10^{-6}$	$7.530 \cdot 10^{-1}$	$7.671 \cdot 10^{-1}$
O_2 Mass Fraction	$6.144 \cdot 10^{-5}$	$6.144 \cdot 10^{-5}$	$2.321 \cdot 10^{-6}$	$9.986 \cdot 10^{-4}$	$6.019 \cdot 10^{-10}$	$9.986 \cdot 10^{-4}$	$1.226 \cdot 10^{-3}$	$2.097 \cdot 10^{-9}$	$1.226 \cdot 10^{-3}$	$1.275 \cdot 10^{-2}$	$7.886 \cdot 10^{-8}$	$2.287 \cdot 10^{-1}$	$2.329 \cdot 10^{-1}$

Stream	*6*	*18*	*17*	*15*	*14*	*16*	*20*	*22*	*Humidity*	*Air*	*19*	*21a*
Mass Flow [kg/s]	$3.232 \cdot 10^{3}$	$3.184 \cdot 10^{1}$	$1.601 \cdot 10^{2}$	6.415	$5.857 \cdot 10^{-2}$	$3.193 \cdot 10^{3}$	$2.925 \cdot 10^{3}$	$2.975 \cdot 10^{3}$	$1.679 \cdot 10^{1}$	$2.778 \cdot 10^{-1}$	$7.678 \cdot 10^{1}$	$1.665 \cdot 10^{2}$
Temperature [°C]	31.19	20.19	20.19	27.79	69.60	20.19	20.19	7.00	20.00	20.00	20.19	20.50
Pressure [kPa]	101.325	100	100	101.3	120	100	100	110	100	101.325	100	100
Molecular Weight	18.02	18.02	18.02	37.07	34.08	18.02	18.02	28.75	18.02	28.85	18.02	18.38
Mass Density [kg/m^3]	1002.67	1010.95	1010.95	1.81	1.44	1010.95	1010.95	1.36	1011.09	1.20	1010.95	47.39
Mass Enhtalpy [kJ/kg]	$-1.586 \cdot 10^{4}$	$-1.591 \cdot 10^{4}$	$-1.591 \cdot 10^{4}$	$-9.030 \cdot 10^{3}$	$-5.484 \cdot 10^{2}$	$-1.591 \cdot 10^{4}$	$-1.591 \cdot 10^{4}$	$-9.435 \cdot 10^{1}$	$-1.591 \cdot 10^{4}$	-5.342	$-1.591 \cdot 10^{4}$	$-1.564 \cdot 10^{4}$
H_2O Mass Fraction	$9.999 \cdot 10^{-1}$	1.000	1.000	$9.624 \cdot 10^{-2}$	0.000	1.000	1.000	$5.642 \cdot 10^{-3}$	1.000	0.000	1.000	$9.652 \cdot 10^{-1}$
H_2S Mass Fraction	$1.816 \cdot 10^{-6}$	$2.787 \cdot 10^{-11}$	$2.787 \cdot 10^{-11}$	$9.140 \cdot 10^{-6}$	1.000	$2.787 \cdot 10^{-11}$	$2.787 \cdot 10^{-11}$	0.000	0.000	0.000	$2.787 \cdot 10^{-11}$	$3.522 \cdot 10^{-7}$
H_2 Mass Fraction	$7.853 \cdot 10^{-11}$	$5.470 \cdot 10^{-22}$	$5.470 \cdot 10^{-22}$	$4.044 \cdot 10^{-4}$	0.000	$5.470 \cdot 10^{-22}$	$5.470 \cdot 10^{-22}$	0.000	0.000	0.000	$5.470 \cdot 10^{-22}$	$1.558 \cdot 10^{-5}$
NH_3 Mass Fraction	$1.088 \cdot 10^{-5}$	$6.584 \cdot 10^{-6}$	$6.584 \cdot 10^{-6}$	$3.327 \cdot 10^{-5}$	0.000	$6.584 \cdot 10^{-6}$	$6.584 \cdot 10^{-6}$	0.000	0.000	0.000	$6.584 \cdot 10^{-6}$	$7.612 \cdot 10^{-6}$
HCl Mass Fraction	0.000	0.000	0.000	0.000	0.000	0.000	0.000	0.000	0.000	0.000	0.000	0.000
Hg Mass Fraction	$1.116 \cdot 10^{-10}$	$4.396 \cdot 10^{-15}$	$4.396 \cdot 10^{-15}$	$4.255 \cdot 10^{-9}$	$4.613 \cdot 10^{-5}$	$4.396 \cdot 10^{-15}$	$4.396 \cdot 10^{-15}$	0.000	0.000	0.000	$4.396 \cdot 10^{-15}$	$1.639 \cdot 10^{-10}$
CH_4 Mass Fraction	$5.906 \cdot 10^{-12}$	$8.841 \cdot 10^{-28}$	$8.841 \cdot 10^{-28}$	$5.109 \cdot 10^{-3}$	0.000	$8.841 \cdot 10^{-28}$	$8.841 \cdot 10^{-28}$	0.000	0.000	0.000	$8.841 \cdot 10^{-28}$	$1.968 \cdot 10^{-4}$
CO_2 Mass Fraction	$5.215 \cdot 10^{-5}$	$8.383 \cdot 10^{-11}$	$8.383 \cdot 10^{-11}$	$8.400 \cdot 10^{-1}$	0.000	$8.383 \cdot 10^{-11}$	$8.383 \cdot 10^{-11}$	0.000	0.000	0.000	$8.383 \cdot 10^{-11}$	$3.237 \cdot 10^{-2}$
N_2 Mass Fraction	$2.283 \cdot 10^{-8}$	$1.635 \cdot 10^{-5}$	$1.635 \cdot 10^{-5}$	$4.689 \cdot 10^{-2}$	0.000	$1.635 \cdot 10^{-5}$	$1.635 \cdot 10^{-5}$	$7.627 \cdot 10^{-1}$	0.000	$7.671 \cdot 10^{-1}$	$1.635 \cdot 10^{-5}$	$1.822 \cdot 10^{-3}$
O_2 Mass Fraction	$6.019 \cdot 10^{-10}$	$9.773 \cdot 10^{-7}$	$9.773 \cdot 10^{-7}$	$1.127 \cdot 10^{-2}$	0.000	$9.773 \cdot 10^{-7}$	$9.773 \cdot 10^{-7}$	$2.316 \cdot 10^{-1}$	0.000	$2.329 \cdot 10^{-1}$	$9.773 \cdot 10^{-7}$	$4.352 \cdot 10^{-4}$